Moving-Water Equilibria Preserving Partial Relaxation Scheme for the Saint-Venant System

Xin Liu*, Xi Chen†, Shi Jin‡, Alexander Kurganov§, and Hui Yu¶

Abstract

We develop a new moving-water equilibria preserving numerical scheme for the Saint-Venant system. The new scheme is designed in two major steps. First, the geometric source term is incorporated into the discharge flux, which results in a hyperbolic system with a global flux. Second, the discharge equation is relaxed so that the nonlinearity is moved into the stiff right-hand side of the added auxiliary equation. The main advantages of the new scheme are that (i) no special treatment of the geometric source term is required and (ii) no nonlinear (cubic) equations should be solved to obtain the point values of the water depth out of the reconstructed equilibrium variables as it must be done in the existing alternative methods. We also develop a hybrid numerical flux, which helps to handle various flow regimes in a stable manner. Several numerical experiments are performed to verify that the proposed scheme is capable of exactly preserving general moving-water steady states and accurately capturing their small perturbations.

Key words: Saint-Venant system of shallow water equations, partial relaxation scheme, well-balanced method, steady-state solutions (equilibria), moving-water and still-water equilibria.

AMS subject classification: 76M12, 65M08, 35L65, 86-08, 86A05.

1 Introduction

The Saint-Venant system of shallow water equations proposed in [16] has been widely used to predict fluid flows in estuaries, oceans, coastal regions, lakes, rivers and channels. It generally describes a depth-averaged thin layer free-surface flow of constant density under hydrostatic

*Department of Mathematics, Southern University of Science and Technology, Shenzhen, 518055, China; xliu111@uottawa.ca

†Department of Mathematics, Southern University of Science and Technology, Shenzhen, 518055, China; 11849453@mail.sustech.edu.cn

‡School of Mathematical Sciences, Institute of Natural Sciences, MOE-LSC, Shanghai Jiao Tong University, Shanghai, 200240, China; shijin-m@sjtu.edu.cn

§Department of Mathematics, Southern University of Science and Technology, Shenzhen, 518055, China and Mathematics Department, Tulane University, New Orleans, LA 70118, USA; kurganov@math.tulane.edu

¶Yau Mathematical Science Center, Tsinghua University, Beijing, 100084, China; huiyu@tsinghua.edu.cn

assumption over a rigid bottom. In the one-dimensional (1-D) case, the Saint-Venant system over irregular frictional bottom reads as

$$\begin{cases} h_t + q_x = 0, \\ q_t + \left(hu^2 + \dfrac{g}{2}h^2\right)_x = -ghB_x - g\dfrac{n^2}{h^{7/3}}|q|q, \end{cases} \tag{1.1}$$

where $h(x,t) \geq 0$ is the water depth, $u(x,t)$ is the depth-averaged velocity, $q(x,t) := h(x,t)u(x,t)$ is the flow discharge, g is the constant gravitational acceleration, $B(x)$ is the bottom topography, and n is the Manning friction coefficient of the bottom.

The system (1.1) is a hyperbolic system of balance laws, which admits both smooth and nonsmooth solutions. A special class of the solutions of (1.1) are steady-state solutions at which $h_t \equiv 0$ and $q_t \equiv 0$ due to that the flux gradient in the second equation in (1.1) is exactly balanced by the geometric and friction source terms. Two major classes of steady states are generally considered in the water flow computations. The first class are the "lake at rest" (still-water) steady states with the zero flow velocity:

$$q \equiv 0, \quad h + B \equiv \text{Const}. \tag{1.2}$$

The second class of steady states are general moving-water steady states at which $q \not\equiv 0$. If the bottom friction is neglected, the general moving-water equilibria are given by

$$q \equiv \text{Const}, \quad E := \frac{u^2}{2} + g(h + B) \equiv \text{Const}, \tag{1.3}$$

where E is the energy. For some particular (moving-water) ($q \not\equiv 0$) steady states, we refer the reader to [12] and references therein. Notice that the still-water steady state (1.2) is a special case of the general moving-water steady state (1.3) with $u \equiv 0$.

Steady states are of great practical importance since many physically relevant solutions of (1.1) are, in fact, small perturbations of steady states. Numerically capturing such solutions is a challenging task since straightforward application of shock-capturing methods may lead to spurious oscillations. Such nonphysical oscillations may strongly disturb the simulation of the physical waves unless a very fine mesh is used, which, in turn, causes high, often unaffordable computational cost. Therefore, it is necessary to design well-balanced numerical methods which guarantee that the discretized numerical flux gradient is exactly balanced by the approximated source terms at both the steady states (1.2) and (1.3), so that the steady-state solutions can be exactly preserved independently of the grid size.

For still-water equilibria preserving numerical methods, the well-balanced property hinges on a special approximation of the bed-slope source term $-ghB_x$. We refer the readers to the non-exhaustive list of references on still-water equilibria preserving numerical methods [1, 2, 3, 18, 21, 25, 26, 28, 29, 33]. Preserving moving-water steady states is substantially more complicated even in the frictionless cases; see, e.g., [4, 5, 8, 9, 19, 20, 24, 25, 32, 34, 35, 40, 41, 42]. The main difficulty is related to the fact that well-balanced approximations of the bed-slope source now need to include terms that are small for smooth solutions, but may become artificially large at discontinuities. In the nonzero friction case, moving-water equilibria preserving numerical methods can be found in, e.g., [6, 8, 12, 25].

In order to overcome the numerical difficulties in designing well-balanced approximations of the bed-slope source term, we follow the idea from [8, 10, 14] and incorporate the source terms

of the discharge equation into its flux and rewrite (1.1) in the following equivalent form:

$$\begin{cases} h_t + q_x = 0, \\ q_t + K_x = 0, \end{cases} \tag{1.4}$$

where

$$K := hu^2 + \frac{g}{2}h^2 + R, \tag{1.5}$$

so that K is a global equilibrium variable with

$$R(x,t) := g\int^x \left[h(\xi,t)B_x(\xi) + \frac{n^2}{h^{7/3}(\xi,t)}|q(\xi,t)|q(\xi,t)\right]\mathrm{d}\xi. \tag{1.6}$$

Accordingly, the general (moving-water) steady states can be expressed in terms of q and K as

$$q \equiv \text{Const}, \quad K \equiv \text{Const}.$$

We note that an idea of incorporating the source terms into the fluxes has also been recently used in the derivation of well-balanced schemes for the two-dimensional models of shallow water equations with Coriolis forces [13] and Euler equations with gravitation [10].

In a moving-water equilibria preserving central-upwind scheme, recently presented in [8], the equilibrium variables K and q are reconstructed to obtain the point values of K and q needed to evaluate the numerical fluxes at cell interfaces. In addition, one needs to compute the point values of h there. This is done by solving cubic equations at each cell interface at every time step. This is not only computationally costly, but also quite challenging near the sonic points; also see [9, 24, 32, 41]. Moreover, the system (1.4)–(1.6) is a hyperbolic system with a global flux, which makes the development of an upwind scheme based on the solution of (generalized) Riemann problems difficult or even impossible. In [17], it was proposed to build a relaxation model for both equations in (1.4) so that one can easily develop an upwind scheme for the linear part of the relaxation system. However, the numerical methods proposed in [17] are not well-balanced.

In order to avoid the aforementioned numerical difficulties, we develop a novel numerical scheme using a partial relaxation technique for the second equation in (1.4). The proposed numerical scheme is well-balanced without any need of a special treatment for the source terms, so that it is capable of exactly preserving both the still-water (1.2) and moving-water (1.3) steady states. Our scheme is based on the system (1.4)–(1.6) with a global flux, while solving cubic equations for computing the point values of h is avoided. In order to deal with different flow regimes, we propose to use the upwind method for the subcritical flow and the central upwind method for the trans- and supercritical flow at each cell interface. A piecewise linear reconstruction with generalized minmod limiter and a second-order steady state and sign preserving semi-implicit Runge-Kutta ODE solver from [11] are used in the developed numerical method to achieve the second order accuracy in both space and time.

The paper is organized as follows. A new partial relaxation approximation of the Saint Venant system is proposed in §2. The numerical scheme based on the hybrid numerical fluxes is derived in §3. The new numerical scheme is tested on a variety of numerical examples in §4.

2 Partial Relaxation Approximation of (1.4)–(1.6)

In this section, we present a relaxation approximation of the Saint-Venant system (1.4)–(1.6).

2.1 A Brief Overview of Relaxation Schemes

We begin with a review of relaxation schemes, which were originally proposed in [22] for systems of conservation laws. These schemes are developed by constructing a linear hyperbolic system with a stiff lower order term that approximates the original system with a small dissipative correction. For the 1-D conservation law of the form

$$\boldsymbol{U}_t + \boldsymbol{F}(\boldsymbol{U})_x = \boldsymbol{0}, \tag{2.1}$$

one can introduce the relaxation approximation

$$\begin{aligned} &\boldsymbol{U}_t + \boldsymbol{P}_x = \boldsymbol{0}, \\ &\boldsymbol{P}_t + a^2\boldsymbol{U}_x = -\frac{1}{\varepsilon}(\boldsymbol{P} - \boldsymbol{F}(\boldsymbol{U})), \end{aligned} \tag{2.2}$$

which is equivalent to the original system (2.1) in the small relaxation limit when the relaxation time $\varepsilon \to 0^+$. In (2.2), $\boldsymbol{P}$ is an introduced auxiliary variable and a is a positive constant satisfying the subcharacteristic condition: $a \geq \max\limits_{\boldsymbol{U}} \rho(\partial \boldsymbol{F}(\boldsymbol{U})/\partial \boldsymbol{U})$, where ρ denotes the spectral radius of the matrix.

In [17], a slightly modified version of the relaxation scheme (2.2), applied to the Saint-Venant system (1.4)–(1.6), resulted in the following relaxation approximation:

$$\begin{aligned} &\boldsymbol{U}_t + \boldsymbol{P}_x = \boldsymbol{0}, \\ &\boldsymbol{P}_t + A^2\boldsymbol{U}_x = -\frac{1}{\varepsilon}\left(\boldsymbol{P} - \boldsymbol{F}(\boldsymbol{U})\right), \end{aligned} \tag{2.3}$$

where

$$\boldsymbol{U} = \begin{pmatrix} h \\ q \end{pmatrix}, \quad \boldsymbol{P} = \begin{pmatrix} w \\ v \end{pmatrix}, \quad A = \begin{pmatrix} a_1 & 0 \\ 0 & a_2 \end{pmatrix}, \quad \boldsymbol{F}(\boldsymbol{U}) = \begin{pmatrix} q \\ K \end{pmatrix}, \tag{2.4}$$

in which the relaxation source term rapidly drives $\boldsymbol{P} \to \boldsymbol{F}(\boldsymbol{U})$ in the limit as $\varepsilon \to 0^+$. One can thus build an upwind semi-discrete approximation of the relaxation system (2.3), (2.4). Its first-order form reads as

$$\frac{d}{\mathrm{d}t}\overline{\boldsymbol{U}}_j + \frac{\overline{\boldsymbol{P}}_{j+1} - \overline{\boldsymbol{P}}_{j-1}}{2\Delta x} = \frac{\Delta x}{2} \cdot A\,\frac{\overline{\boldsymbol{U}}_{j+1} - 2\overline{\boldsymbol{U}}_j + \overline{\boldsymbol{U}}_{j-1}}{(\Delta x)^2}, \tag{2.5}$$

$$\frac{\mathrm{d}}{\mathrm{d}t}\overline{\boldsymbol{P}}_j + A^2\,\frac{\overline{\boldsymbol{U}}_{j+1} - \overline{\boldsymbol{U}}_{j-1}}{2\Delta x} = -\frac{1}{\varepsilon}\left(\overline{\boldsymbol{P}} - \boldsymbol{F}(\overline{\boldsymbol{U}})\right) + \frac{\Delta x}{2} \cdot \frac{\overline{\boldsymbol{P}}_{j+1} - 2\overline{\boldsymbol{P}}_j + \overline{\boldsymbol{P}}_{j-1}}{(\Delta x)^2}. \tag{2.6}$$

Unfortunately, the numerical scheme (2.5), (2.6) as well as its higher-order modifications introduced in [17] are not well-balanced since the dissipative terms on the right-hand side (RHS) of (2.5) and (2.6) do not vanish at steady states and thus introduce spurious waves.

2.2 Partial Relaxation System

In order to construct a well-balanced relaxation scheme for the system (1.4)–(1.6), we introduce the following *partial relaxation system* in which we only relax the second equation in (1.4):

$$h_t + q_x = 0, \tag{2.7}$$
$$q_t + v_x = 0, \tag{2.8}$$
$$v_t + a^2 q_x = -\frac{1}{\varepsilon}(v - K), \tag{2.9}$$

in which v is an auxiliary variable. In the numerical results reported in §4, we have used $\varepsilon = 10^{-6}$. Such a relaxation is similar to the Suliciu's relaxation [36], which also found other applications, see for example [15].

In the small relaxation limit ($\varepsilon \to 0^+$), equations (2.8) and (2.9) can be approximated to leading order by

$$v = K, \quad q_t + K_x = 0, \tag{2.10}$$

and one can find that the local equilibrium (2.10) is the momentum equation in (1.4).

It is well-known that the relaxation approximation is dissipative and thus well-posed provided a is sufficiently large, that is, it satisfies a subcharacteristic condition which is derived below. In order to establish a proper subcharacteristic condition for the partial relaxation system (2.7)–(2.9), we consider a simple case with $B \equiv \text{Const}$ and $n = 0$ (that is, the case in which the RHS of (1.1) vanishes) in our analysis. In this case,

$$K = hu^2 + \frac{g}{2}h^2 = \frac{q^2}{h} + \frac{g}{2}h^2, \tag{2.11}$$

and thus

$$K_x = 2uq_x - (u^2 - gh)h_x. \tag{2.12}$$

Nest, using (2.10)–(2.12), we obtain

$$K_t = 2uq_t - (u^2 - gh)h_t = -2uK_x - (u^2 - gh)h_t = 2u(u^2 - gh)h_x - (3u^2 + gh)q_x.$$

We then use the Chapman-Enskog expansion [7], one can obtain the following first-order approximation of the proposed partial relaxation system (2.7)–(2.9):

$$v = K - \varepsilon\left[2u(u^2 - gh)h_x + (a^2 - 3u^2 - gh)q_x\right] + \mathcal{O}(\varepsilon^2),$$

which can be then substituted into (2.8) to eliminate the auxiliary variable v. This results in

$$\begin{pmatrix} h \\ q \end{pmatrix}_t + \begin{pmatrix} q \\ K \end{pmatrix}_x = \varepsilon\left[\begin{pmatrix} 0 & 0 \\ 2u(u^2 - gh) & a^2 - 3u^2 - gh \end{pmatrix}\begin{pmatrix} h \\ q \end{pmatrix}_x\right]_x + \begin{pmatrix} 0 \\ \mathcal{O}(\varepsilon^2) \end{pmatrix}, \tag{2.13}$$

which introduces a higher-order dissipative perturbation of the system (1.4)–(1.6). As one can easily see, the system (2.13) is dissipative provided the following subcharacteristic condition is satisfied:

$$a > \sqrt{3u^2 + gh}. \tag{2.14}$$

3 Numerical Scheme

In this section, we develop a semi-discrete numerical scheme for the partially relaxed system (2.7)–(2.9), which can be rewritten in the following vector form:

$$\boldsymbol{U}_t + \boldsymbol{F}(\boldsymbol{U})_x = \boldsymbol{S}(\boldsymbol{U}), \tag{3.1}$$

where

$$\boldsymbol{U} = \begin{pmatrix} h \\ q \\ v \end{pmatrix}, \quad \boldsymbol{F}(\boldsymbol{U}) = \begin{pmatrix} q \\ v \\ a^2 q \end{pmatrix}, \quad \boldsymbol{S}(\boldsymbol{U}) = \begin{pmatrix} 0 \\ 0 \\ -\dfrac{1}{\varepsilon}(v-K) \end{pmatrix}. \tag{3.2}$$

The computational domain is discretized using the finite-volume cells $I_j = [x_{j-\frac{1}{2}}, x_{j+\frac{1}{2}}]$ of size Δx centered at $x_j = \big(x_{j-\frac{1}{2}} + x_{j+\frac{1}{2}}\big)/2$ with $j = j_\ell, \ldots, j_r$. We assume that the cell averages of $\boldsymbol{U}$,

$$\overline{\boldsymbol{U}}_j(t) \approx \frac{1}{\Delta x}\int\limits_{I_j} \boldsymbol{U}(x,t)\,\mathrm{d}x, \tag{3.3}$$

are available at a certain time level t and define the cell averages of $\boldsymbol{S}$ by

$$\overline{\boldsymbol{S}}_j(t) \approx \frac{1}{\Delta x}\int\limits_{I_j} \boldsymbol{S}(\boldsymbol{U}(x,t))\,\mathrm{d}x.$$

We note that in the semi-discrete framework, all of the indexed quantities that depend on $\boldsymbol{U}$ automatically depend on t, but we will omit this time-dependence in the rest of the paper for the sake of brevity.

3.1 Piecewise Linear Reconstruction and Point Values

Adopting the second-order finite-volume approach, we use the cell averages (3.3) to approximate the computed solution using a second-order piecewise linear reconstruction

$$\widetilde{\boldsymbol{U}}(x) := \overline{\boldsymbol{U}}_j + (\boldsymbol{U}_x)_j(x - x_j), \quad x \in I_j, \tag{3.4}$$

where the slopes $\boldsymbol{U}_x$ are to be computed in a non-oscillatory manner using a nonlinear limiter. In the numerical results reported in §4, we have used the generalized minmod limiter (see, e.g., [30, 31, 37, 38]):

$$(\boldsymbol{U}_x)_j = \mathrm{minmod}\left(\theta\,\frac{\boldsymbol{U}_{j+1} - \boldsymbol{U}_j}{\Delta x}, \frac{\boldsymbol{U}_{j+1} - \boldsymbol{U}_{j-1}}{2\Delta x}, \theta\,\frac{\boldsymbol{U}_j - \boldsymbol{U}_{j-1}}{\Delta x}\right),$$

with the minmod function

$$\mathrm{minmod}(z_1, z_2, \cdots) := \begin{cases} \min(z_1, z_2, \cdots), & \text{if } z_i > 0 \ \ \forall i, \\ \max(z_1, z_2, \cdots), & \text{if } z_i < 0 \ \ \forall i, \\ 0, & \text{otherwise.} \end{cases}$$

The parameter $\theta \in [1,2]$ controls the amount of numerical dissipation: the larger the θ, the smaller the numerical dissipation.

Using the piecewise linear reconstruction (3.4), we obtain the left- and right-sided point values of $\boldsymbol{U}$ by

$$\boldsymbol{U}^-_{j+\frac{1}{2}} = \overline{\boldsymbol{U}}_j + \frac{\Delta x}{2}(\boldsymbol{U}_x)_j, \quad \boldsymbol{U}^+_{j+\frac{1}{2}} = \overline{\boldsymbol{U}}_{j+1} - \frac{\Delta x}{2}(\boldsymbol{U}_x)_{j+1}.$$

These values can be then used to compute the corresponding values of $u = q/h$. In order to be able to simulate the flows near wet-dry fronts, we use the desingularization procedure to compute the point value of velocity (see, e.g., [25, 28]), namely,

$$u^\pm_{j+\frac{1}{2}} = \frac{\sqrt{2}h^\pm_{j+\frac{1}{2}}q^\pm_{j+\frac{1}{2}}}{\sqrt{\left(h^\pm_{j+\frac{1}{2}}\right)^4 + \max\left\{\left(h^\pm_{j+\frac{1}{2}}\right)^4, \tau\right\}}},$$

where $\tau > 0$ is prescribed positive parameter which is used to avoid division by very small numbers. In the numerical experiments reported in §4, we have used $\tau = 10^{-10}$. For consistency, we then recompute the corresponding values of q by

$$q^\pm_{j+\frac{1}{2}} = h^\pm_{j+\frac{1}{2}} \cdot u^\pm_{j+\frac{1}{2}}.$$

Equipped with the reconstructed point values of h and u, we use (2.14) and the eigenvalues of the Jacobian of the original Saint-Venant system (1.1) to set

$$\begin{aligned} a = \max_j \Big\{ \max\Big(&|u^+_{j+\frac{1}{2}}| + \sqrt{gh^+_{j+\frac{1}{2}}},\ |u^-_{j+\frac{1}{2}}| + \sqrt{gh^-_{j+\frac{1}{2}}},\\ &\sqrt{3(u^+_{j+\frac{1}{2}})^2 + gh^+_{j+\frac{1}{2}}},\ \sqrt{3(u^-_{j+\frac{1}{2}})^2 + gh^-_{j+\frac{1}{2}}}\Big)\Big\} \end{aligned} \tag{3.5}$$

Notice that a is to be recomputed at every time step.

3.2 Source Term Evaluation

The third component of the source term $\boldsymbol{S}_j$ is computed using the midpoint quadrature:

$$\overline{S}^{(3)}_j = -\frac{1}{\varepsilon}\left(\bar{v}_j - K_j\right),$$

where the values of the global variable K at the cell centers x_j are computed by

$$K_j = \frac{\sqrt{2}\,\bar{h}_j\bar{q}^2_j}{\bar{h}^4_j + \max\left\{\bar{h}^4_j, \tau\right\}} + \frac{g}{2}\bar{h}^2_j + R_j, \quad j = j_\ell, \ldots, j_r. \tag{3.6}$$

Here, R_j can be computed using (1.6):

$$R_j = R(x_j,t) = g\int^{x_j}\left[h(\xi,t)B_x(\xi) + \frac{n^2}{h^{7/3}(\xi,t)}|q(\xi,t)|q(\xi,t)\right]\mathrm{d}\xi, \quad j = j_\ell, \ldots, j_r. \tag{3.7}$$

We notice that the formula (3.7) can be rewritten in the following recursive way:

$$R_j = R_{j-1} + g \int_{x_{j-1}}^{x_j} \left[h(\xi,t)B_x(\xi) + \frac{n^2}{h^{7/3}(\xi,t)}|q(\xi,t)|q(\xi,t) \right] \mathrm{d}\xi, \quad j = j_\ell + 1, \ldots, j_r, \tag{3.8}$$

and then the integral in (3.8) is discretized using a second-order quadrature to obtain

$$\begin{aligned} R_j = {} & R_{j-1} + \frac{g}{2}(\bar{h}_{j-1} + \bar{h}_j)(B_j - B_{j-1}) \\ & + \frac{gn^2}{2} \left[\frac{\sqrt{2}\,\bar{h}_{j-1}|\bar{q}_{j-1}|\bar{q}_{j-1}}{\left(\bar{h}_{j-1}^4 + \max\left\{\bar{h}_{j-1}^4, \tau\right\}\right)^{5/6}} + \frac{\sqrt{2}\,\bar{h}_j|\bar{q}_j|\bar{q}_j}{\left(\bar{h}_j^4 + \max\left\{\bar{h}_j^4, \tau\right\}\right)^{5/6}} \right] \Delta x, \ j = j_\ell + 1, \ldots, j_r. \end{aligned} \tag{3.9}$$

It should be observed that the recursive formula (3.9) requires a starting value R_1, which is obtained by setting $R_1 := (R_{\frac{1}{2}} + R_{\frac{3}{2}})/2$, where $R_{\frac{1}{2}} := 0$ and $R_{\frac{3}{2}}$ is computed using a slightly different quadrature:

$$R_{\frac{3}{2}} = g\bar{h}_1(B_{\frac{3}{2}} - B_{\frac{1}{2}}) + \frac{\sqrt{2}\,gn^2\bar{h}_1|\bar{q}_1|\bar{q}_1}{\left(\bar{h}_1^4 + \max\left\{\bar{h}_1^4, \tau\right\}\right)^{5/6}}.$$

3.3 Upwind Numerical Fluxes

A semi-discrete finite-volume method for (3.1), (3.2) can be written as

$$\frac{\mathrm{d}}{\mathrm{d}t}\overline{\boldsymbol{U}}_j = -\frac{\boldsymbol{\mathcal{F}}_{j+\frac{1}{2}} - \boldsymbol{\mathcal{F}}_{j-\frac{1}{2}}}{\Delta x} + \overline{\boldsymbol{S}}_j, \tag{3.10}$$

where $\boldsymbol{\mathcal{F}}_{j+\frac{1}{2}}$ are the numerical fluxes at the cell interfaces.

We note that equation in (2.7) is, in fact, coupled with equations (2.8) and (2.9) through the source term only. We therefore first consider the subsystem

$$\begin{pmatrix} q \\ v \end{pmatrix}_t + \begin{pmatrix} 0 & 1 \\ a^2 & 0 \end{pmatrix} \begin{pmatrix} q \\ v \end{pmatrix}_x = \begin{pmatrix} 0 \\ -\dfrac{1}{\varepsilon}(v - K) \end{pmatrix}. \tag{3.11}$$

Since the left-hand side of (3.11) is linear with constant coefficient, one can easily derive upwind numerical fluxes $\mathcal{F}^{(2)}_{j+\frac{1}{2}}$ and $\mathcal{F}^{(3)}_{j+\frac{1}{2}}$, which read as

$$\mathcal{F}^{(2)}_{j+\frac{1}{2}} = \frac{v^+_{j+\frac{1}{2}} + v^-_{j+\frac{1}{2}}}{2} - \frac{a}{2}\left(q^+_{j+\frac{1}{2}} - q^-_{j+\frac{1}{2}}\right), \tag{3.12}$$

$$\mathcal{F}^{(3)}_{j+\frac{1}{2}} = a^2\,\frac{q^+_{j+\frac{1}{2}} + q^-_{j+\frac{1}{2}}}{2} - \frac{a}{2}\left(v^+_{j+\frac{1}{2}} - v^-_{j+\frac{1}{2}}\right). \tag{3.13}$$

We then use the relation $F^{(3)} = a^2F^{(1)}$ to obtain the remaining component of the numerical flux:

$$\mathcal{F}^{(1)}_{j+\frac{1}{2}} = \frac{q^+_{j+\frac{1}{2}} + q^-_{j+\frac{1}{2}}}{2} - \frac{1}{2a}\left(v^+_{j+\frac{1}{2}} - v^-_{j+\frac{1}{2}}\right). \tag{3.14}$$

3.4 Modified Equation Analysis

We now analyze the stability of the developed semi-discrete upwind scheme using a modified equation analysis. To this end, we take the zero-relaxation limit, in which $\bar{v}_j = K_j$, use the first-order piecewise constant reconstruction obtained by setting $\boldsymbol{U}_j \equiv 0$ in (3.4), and substitute the numerical fluxes $\boldsymbol{\mathcal{F}}_{j+\frac{1}{2}}$ and $\boldsymbol{\mathcal{F}}_{j-\frac{1}{2}}$ into (3.10) to obtain

$$\frac{\mathrm{d}}{\mathrm{d}t}\bar{h}_j + \frac{\bar{q}_{j+1} - \bar{q}_{j-1}}{2\Delta x} = \frac{\Delta x}{2a}\cdot\frac{K_{j+1} - 2K_j + K_{j-1}}{(\Delta x)^2},$$
$$\frac{\mathrm{d}}{\mathrm{d}t}\bar{q}_j + \frac{K_{j+1} - K_{j-1}}{2\Delta x} = \frac{a\Delta x}{2}\cdot\frac{\bar{q}_{j+1} - 2\bar{q}_j + \bar{q}_{j-1}}{(\Delta x)^2}.$$

Thus, the modified equations for the first-order semi-discrete upwind scheme are

$$h_t + q_x = \frac{\Delta x}{2a}\,K_{xx}, \tag{3.15}$$
$$q_t + K_x = \frac{a\Delta x}{2}\,q_{xx}. \tag{3.16}$$

For simplicity, we consider the case with $B \equiv$ Const and $n = 0$, in which K is given by (2.11). We then differentiate equation (2.12) with respect to x to obtain

$$K_{xx} = 2uq_{xx} + (gh - u^2)h_{xx} + \frac{2}{h}(q_x)^2 + \left[\frac{2u}{h} + g\right](h_x)^2 - \frac{4u}{h}q_x h_x,$$

which we substitute into (3.15) and rewrite the modified equations in the following vector form:

$$\begin{pmatrix} h \\ q \end{pmatrix}_t + \begin{pmatrix} q \\ v \end{pmatrix}_x = \frac{\Delta x}{2a}\begin{pmatrix} gh - u^2 & 2u \\ 0 & a^2 \end{pmatrix}\begin{pmatrix} h \\ q \end{pmatrix}_{xx} + \begin{pmatrix} \frac{2}{h}(q_x)^2 + \left[\frac{2u}{h} + g\right](h_x)^2 - \frac{4u}{h}q_x h_x \\ 0 \end{pmatrix}. \tag{3.17}$$

As one can see, the system (3.17) is dissipative as long as

$$|u| < \sqrt{gh}, \tag{3.18}$$

which is true for subcritical flows only. This indicates that the upwind numerical flux approximations (3.12)–(3.14) may lead to a stable approximate solution only under the subcritical flow condition (3.18).

Remark 3.1 We have conducted a series of numerical experiments (not reported in this paper), which clearly indicate that the developed partial relaxation scheme based on the upwind fluxes (3.12)–(3.14) is indeed unstable in the supercritical flow regime.

3.5 Hybrid Upwind/Central-Upwind Numerical Fluxes

According to the analysis in §3.4, at those cell interfaces $x = x_{j+\frac{1}{2}}$, where either

$$u^+_{j+\frac{1}{2}} > \sqrt{gh^+_{j+\frac{1}{2}}} \quad \text{or} \quad u^-_{j+\frac{1}{2}} > \sqrt{gh^-_{j+\frac{1}{2}}},$$

we replace the upwind numerical fluxes (3.12)–(3.14) with the central-upwind ones, originally developed in [27] for general hyperbolic systems of conservation laws:

$$\boldsymbol{\mathcal{F}}_{j+\frac{1}{2}} = \frac{a^+_{j+\frac{1}{2}}\boldsymbol{F}(\boldsymbol{U}^-_{j+\frac{1}{2}}) - a^-_{j+\frac{1}{2}}\boldsymbol{F}(\boldsymbol{U}^+_{j+\frac{1}{2}})}{a^+_{j+\frac{1}{2}} - a^-_{j+\frac{1}{2}}} + \frac{a^+_{j+\frac{1}{2}}a^-_{j+\frac{1}{2}}}{a^+_{j+\frac{1}{2}} - a^-_{j+\frac{1}{2}}}\left(\boldsymbol{U}^+_{j+\frac{1}{2}} - \boldsymbol{U}^-_{j+\frac{1}{2}}\right). \tag{3.19}$$

Here, $a^+_{j+\frac{1}{2}}$ and $a^-_{j+\frac{1}{2}}$ are one-sided local speeds of propagation. Their careful estimation allows one to control the amount of the numerical diffusion present in the central-upwind flux. If one wants to apply the central-upwind flux in all of the flow regimes (both sub- and supercritical), one has to set $a^+_{j+\frac{1}{2}} = -a^-_{j+\frac{1}{2}} \equiv a$ for all j, which would lead to a very diffusive and non-well-balanced discretization of the system (2.7)–(2.9). However, as we use the central-upwind flux in the supercritical regime only, we can safely estimate the one-sided local speeds in (3.19) by using the largest and smallest eigenvalues of the original system (1.1), namely, by setting

$$\begin{aligned}
a^+_{j+\frac{1}{2}} &= \max\left\{u^+_{j+\frac{1}{2}} + \sqrt{gh^+_{j+\frac{1}{2}}}, u^-_{j+\frac{1}{2}} + \sqrt{gh^-_{j+\frac{1}{2}}}, 0\right\},\\
a^-_{j+\frac{1}{2}} &= \min\left\{u^+_{j+\frac{1}{2}} - \sqrt{gh^+_{j+\frac{1}{2}}}, u^-_{j+\frac{1}{2}} - \sqrt{gh^-_{j+\frac{1}{2}}}, 0\right\}.
\end{aligned}$$

Remark 3.2 We note that the presented flux hybridization does not guarantee the positivity of the computed water depth. In order to enforce the positivity, we modify the first component of the numerical fluxes, $\mathcal{F}^{(1)}_{j+\frac{1}{2}}$ using the "draining" time-step strategy proposed in [3] (also see [2, 8, 9]).

3.6 Fully Discrete Semi-Implicit Scheme

The semi-discretization (3.10) results in a system of time-dependent ODEs, which should be solved using an efficient, stable and sufficiently accurate ODE solver. Since the source term in (3.10) is stiff, explicit ODE solvers typically used for solving nonlinear hyperbolic systems may be extremely inefficient as they suffer of severe stability time-step restrictions. We therefore implement the second-order steady state and sign preserving semi-implicit Runge-Kutta ODE solver SI-RK3 from [11, equation (3.2)]. In this section, we provide all of the required details as application of the SI-RK3 method to the ODE system (3.10) is not straightforward due to the presence of the non-damping source term K/ε.

Let us assume that at time level $t = t^m$ the computed cell averages, $\{\bar{h}^m_j\}$, $\{\bar{q}^m_j\}$ and $\{\bar{v}^m_j\}$, are available. We then evolve them to the next time level $t = t^{m+1} = t^m + \Delta t^m$ according to the following algorithm.

Step 1. Compute a by (3.5) and use it to evaluate

$$\Delta t^m = C\,\frac{\Delta x}{a},$$

where C is a CFL number. In the numerical results reported in §4, we have used $C = 0.4$.
Step 2. Use $\{\bar{h}_j^m\}$, $\{\bar{q}_j^m\}$ and $\{\bar{v}_j^m\}$ to compute $\{\boldsymbol{\mathcal{F}}_{j+\frac{1}{2}}^m\}$ according to §3.1, §3.3 and §3.5.
Step 3. Compute

$$\bar{h}_j^I = \bar{h}_j^m - \frac{\Delta t^m}{\Delta x}\left(\mathcal{F}_{j+\frac{1}{2}}^{m,(1)} - \mathcal{F}_{j-\frac{1}{2}}^{m,(1)}\right),$$
$$\bar{q}_j^I = \bar{q}_j^m - \frac{\Delta t^m}{\Delta x}\left(\mathcal{F}_{j+\frac{1}{2}}^{m,(2)} - \mathcal{F}_{j-\frac{1}{2}}^{m,(2)}\right).$$

Step 4. Use $\{\bar{h}_j^I\}$ and $\{\bar{q}_j^I\}$ to compute $\{K_j^I\}$ by (3.6), (3.9).
Step 5. Compute

$$\bar{v}_j^I = \frac{\varepsilon}{\varepsilon + \Delta t^m}\left[\bar{v}_j^m - \frac{\Delta t^m}{\Delta x}\left(\mathcal{F}_{j+\frac{1}{2}}^{m,(3)} - \mathcal{F}_{j-\frac{1}{2}}^{m,(3)}\right) + \frac{\Delta t^m}{\varepsilon}K_j^I\right].$$

Step 6. Use $\{\bar{h}_j^I\}$, $\{\bar{q}_j^I\}$ and $\{\bar{v}_j^I\}$ to compute $\{\boldsymbol{\mathcal{F}}_{j+\frac{1}{2}}^I\}$ according to §3.1, §3.3 and §3.5.
Step 7. Compute

$$\bar{h}_j^{II} = \frac{3}{4}\bar{h}_j^m + \frac{1}{4}\left[\bar{h}_j^I - \frac{\Delta t^m}{\Delta x}\left(\mathcal{F}_{j+\frac{1}{2}}^{I,(1)} - \mathcal{F}_{j-\frac{1}{2}}^{I,(1)}\right)\right],$$
$$\bar{q}_j^{II} = \frac{3}{4}\bar{q}_j^m + \frac{1}{4}\left[\bar{q}_j^I - \frac{\Delta t^m}{\Delta x}\left(\mathcal{F}_{j+\frac{1}{2}}^{I,(2)} - \mathcal{F}_{j-\frac{1}{2}}^{I,(2)}\right)\right].$$

Step 8. Use $\{\bar{h}_j^{II}\}$ and $\{\bar{q}_j^{II}\}$ to compute $\{K_j^{II}\}$ by (3.6), (3.9).
Step 9. Compute

$$\bar{v}_j^{II} = \frac{3}{4}\bar{v}_j^m + \frac{\varepsilon}{4(\varepsilon + \Delta t^m)}\left[\bar{v}_j^I - \frac{\Delta t^m}{\Delta x}\left(\mathcal{F}_{j+\frac{1}{2}}^{I,(3)} - \mathcal{F}_{j-\frac{1}{2}}^{I,(3)}\right) + \frac{\Delta t^m}{\varepsilon}K_j^{II}\right].$$

Step 10. Use $\{\bar{h}_j^{II}\}$, $\{\bar{q}_j^{II}\}$ and $\{\bar{v}_j^{II}\}$ to compute $\{\boldsymbol{\mathcal{F}}_{j+\frac{1}{2}}^{II}\}$ according to §3.1, §3.3 and §3.5.
Step 11. Compute

$$\bar{h}_j^{m+1} = \frac{1}{3}\bar{h}_j^m + \frac{2}{3}\left[\bar{h}_j^{II} - \frac{\Delta t^m}{\Delta x}\left(\mathcal{F}_{j+\frac{1}{2}}^{II,(1)} - \mathcal{F}_{j-\frac{1}{2}}^{II,(1)}\right)\right],$$
$$\bar{q}_j^{m+1} = \frac{1}{3}\bar{q}_j^m + \frac{2}{3}\left[\bar{q}_j^{II} - \frac{\Delta t^m}{\Delta x}\left(\mathcal{F}_{j+\frac{1}{2}}^{II,(2)} - \mathcal{F}_{j-\frac{1}{2}}^{II,(2)}\right)\right].$$

Step 12. Use $\{\bar{h}_j^{m+1}\}$ and $\{\bar{q}_j^{m+1}\}$ to compute $\{K_j^{m+1}\}$ by (3.6), (3.9).
Step 13. Compute

$$\bar{v}_j^{III} = \frac{1}{3}\bar{v}_j^m + \frac{2\varepsilon}{3(\varepsilon + \Delta t^m)}\left[\bar{v}_j^{II} - \frac{\Delta t^m}{\Delta x}\left(\mathcal{F}_{j+\frac{1}{2}}^{II,(3)} - \mathcal{F}_{j-\frac{1}{2}}^{II,(3)}\right) + \frac{\Delta t^m}{\varepsilon}K_j^{m+1}\right].$$

Step 14. Use $\{\bar{h}_j^{m+1}\}$, $\{\bar{q}_j^{m+1}\}$ and $\{\bar{v}_j^{III}\}$ to compute $\{\mathcal{F}_{j+\frac{1}{2}}^{III,(3)}\}$ according to §3.1, §3.3 and §3.5.
Step 15. Compute

$$\bar{v}_j^{m+1} = \frac{\varepsilon^2}{\varepsilon^2 + (\Delta t^m)^2}\left[\bar{v}_j^{III} - \frac{(\Delta t^m)^2}{\varepsilon \Delta x}\left(\mathcal{F}_{j+\frac{1}{2}}^{III,(3)} - \mathcal{F}_{j-\frac{1}{2}}^{III,(3)}\right) + \left(\frac{\Delta t^m}{\varepsilon}\right)^2 K_j^{m+1}\right].$$

4 Numerical Examples

In this section, we test the performance of the proposed well-balanced partial relaxation scheme on a number of numerical examples. In these tests, we consider the cases of both continuous and discontinuous bottom topographies. In all of the examples, we perform computations in the computational domain $[0, 25]$ split into N uniform cells with simple transmissive boundary conditions and use the following parameters: the gravitational acceleration $g = 9.812$ and the minmod parameter $\theta = 1.9$.

4.1 Frictionless Saint-Venant System ($n = 0$)

We first consider a frictionless case, for which the Manning friction coefficient $n = 0$.

Example 1—Convergence to Steady States

In this numerical example, we study the convergence of the solutions computed using the proposed partial relaxation scheme towards steady flow over a hump. The bottom topography function is continuous and defined by

$$B(x) = \begin{cases} 0.2 - 0.05(x-10)^2, & \text{if } \ 8 \le x \le 12, \\ 0, & \text{otherwise.} \end{cases} \tag{4.1}$$

Depending on the initial and boundary conditions, the flow may be subcritical, supercritical and transcritical with or without a steady shock. We consider the following four sets of initial and boundary data taken from [9] (also see [23, 39]):

(a) *Supercritical flow* with

$$\begin{aligned} &h(x,0) = 2 - B(x), \quad q(x,0) \equiv 0, \\ &h(0,t) = 2, \quad q(0,t) = 24; \end{aligned} \tag{4.2}$$

(b) *Subcritical flow* with

$$\begin{aligned} &h(x,0) = 2 - B(x), \quad q(x,0) \equiv 0, \\ &q(0,t) = 4.42, \quad h(25,t) = 2; \end{aligned} \tag{4.3}$$

(c) *Transcritical flow without a jump* with

$$\begin{aligned} &h(x,0) = 0.66 - B(x), \quad q(x,0) \equiv 0, \\ &q(0,t) = 1.53, \quad h(25,t) = 0.66; \end{aligned} \tag{4.4}$$

(d) *Transcritical flow with a jump* with

$$\begin{aligned} &h(x,0) = 0.33 - B(x), \quad q(x,0) \equiv 0, \\ &q(0,t) = 0.18, \quad h(25,t) = 0.33. \end{aligned} \tag{4.5}$$

Remark 4.1 In Case (c), the downstream boundary condition ($h(25,t) = 0.66$) is imposed only when the flow is subcritical.

In all of these four cases, the numerical solutions are obtained by the proposed partial relaxation schemes at $t = 300$ using $N = 200$ uniform cells. The results ($h + B$, q, K and E) are shown in Figures 4.1–4.4. As one can see, the proposed numerical scheme can capture the steady states of different flow regimes, and the computed solutions are comparable with those reported in [8, 9, 23, 39].

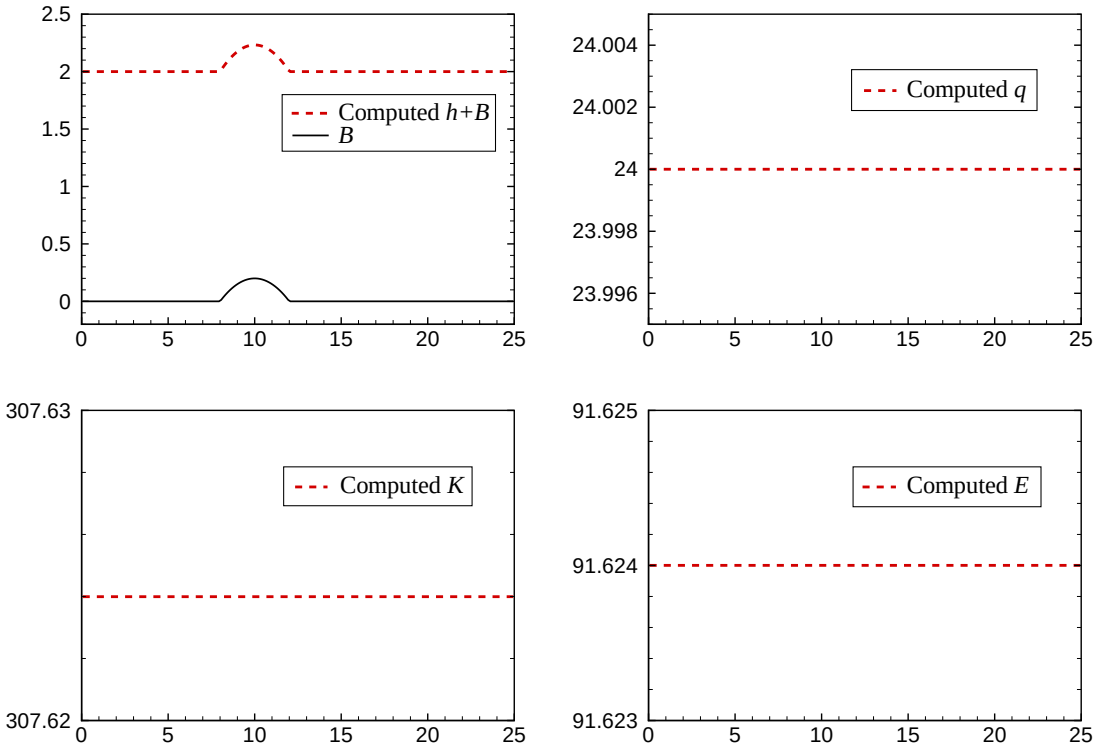

Figure 4.1: Example 1, Case (a): Computed $h + B$, q, K and E.

Example 2—Small Perturbations of Moving-Water Equilibria

This example is designed to test the capability of the proposed numerical scheme of capturing small perturbations of the moving-water equilibria studied in Example 1 over the continuous bottom topography function (4.1). The initial conditions in different flow regimes of this test are taken from the steady state solutions of Cases (a)–(c) in Example 1 with adding a small positive number 0.05 to the water depth in the interval $x \in [5.75, 6.25]$. Theoretically, this disturbance should split into two waves propagating with the flows. We run the tests with 200 uniform cells. We note that the same perturbations of the steady-state solutions were considered in [42].

We compute the numerical solutions using the proposed numerical scheme until the final times $t = 1$ in Case (a) and $t = 1.5$ in Cases (b) and (c) over a coarse and fine meshes with $N = 100$ and 1000 uniform cells, respectively. The obtained results are plotted in Figures 4.5–4.7. As one can observe, no spurious oscillations are generated and the propagating perturbations are well captured over both the coarse and fine meshes.

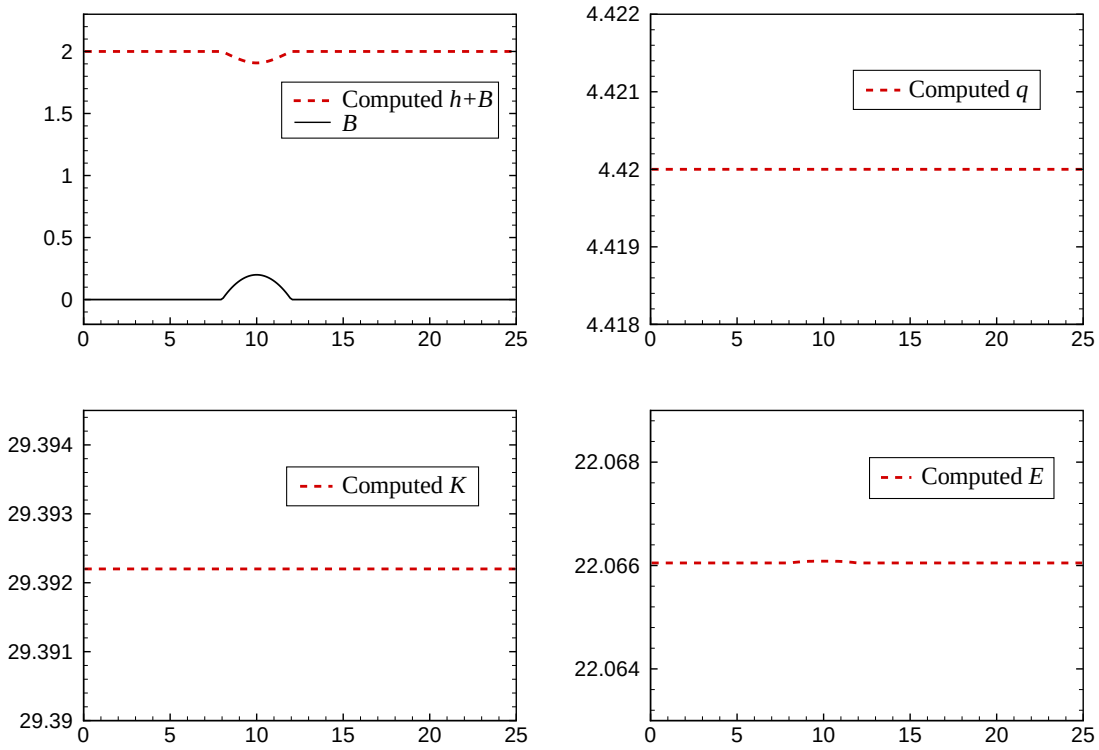

Figure 4.2: Example 1, Case (b): Computed $h + B$, q, K and E.

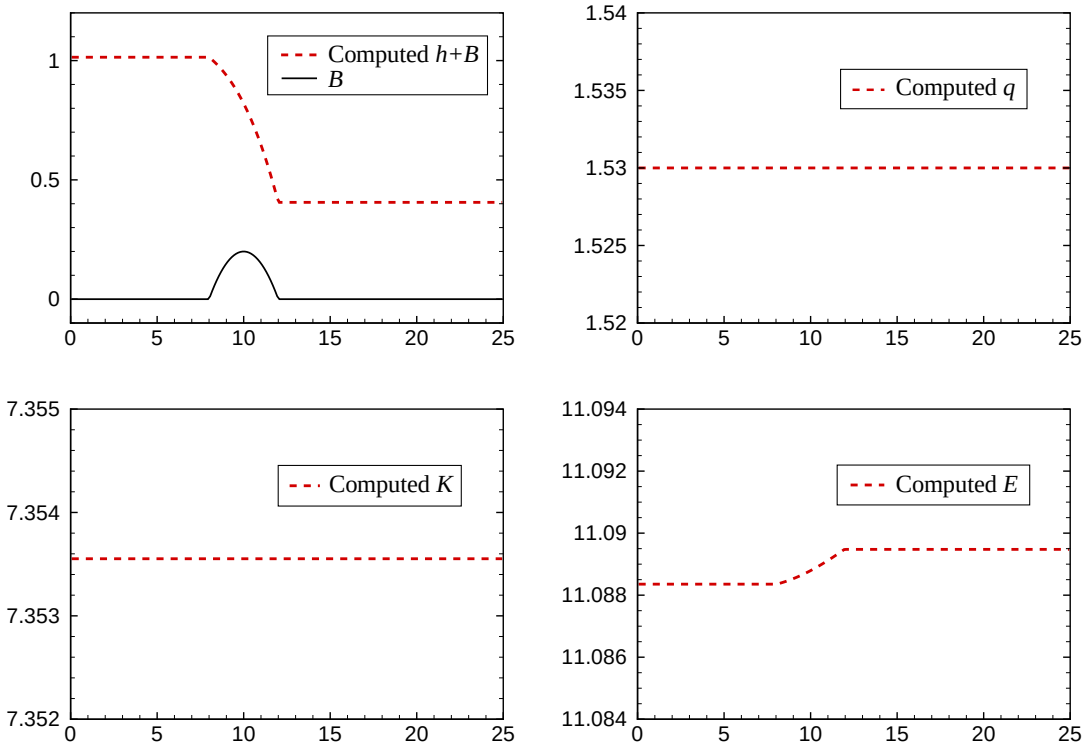

Figure 4.3: Example 1, Case (c): Computed $h + B$, q, K and E.

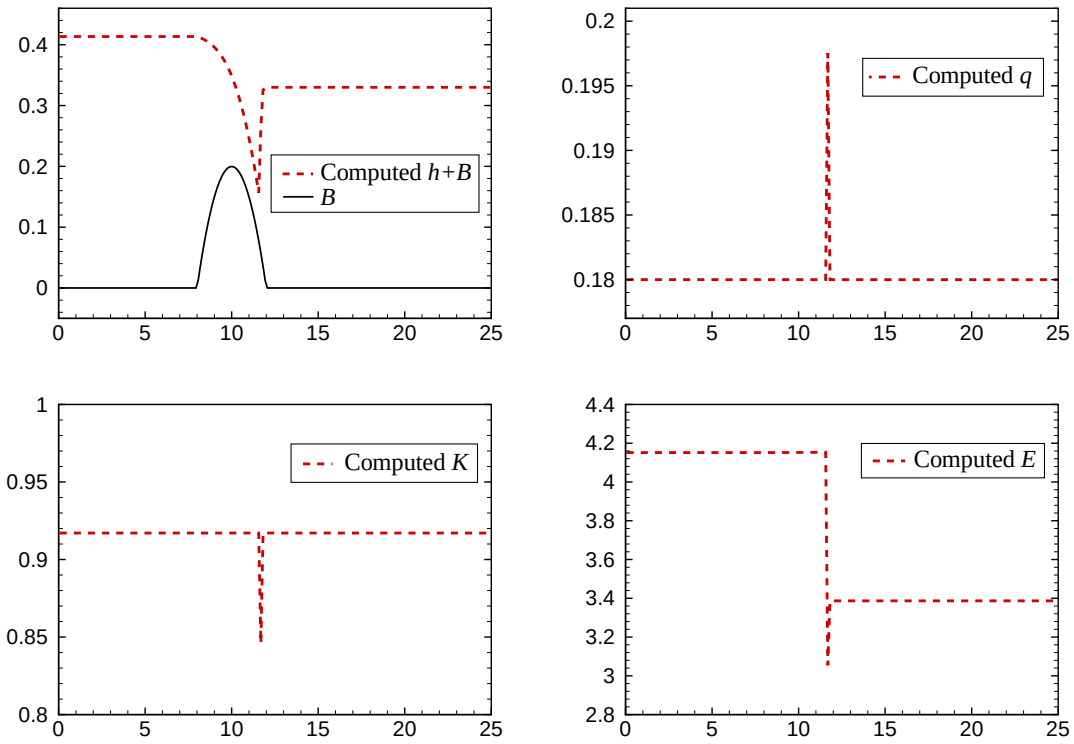

Figure 4.4: Example 1, Case (d): Computed $h + B$, q, K and E.

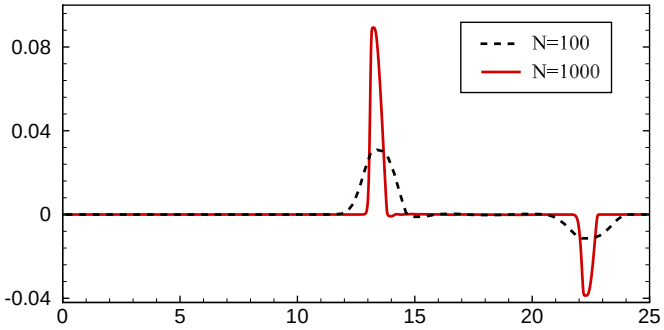

Figure 4.5: Example 2, Case (a): The difference between h and the background moving steady-state water depth computed using 100 and 1000 uniform cells.

4.2 Saint-Venant System with Friction ($n \neq 0$)

We now test the proposed partial relaxation scheme in the presence of the Manning friction term and we set $n = 0.05$. Examples 4–8 below are taken from [8].

Example 3—Accuracy Test

In this example, we modify the test taken from [28, 32] by adding the bottom friction. We verify the convergence rate of the proposed partial relaxation schemes in the case of a smooth solution. The following initial data and the bottom topography

$$h(x,0) = 5 + e^{\cos(2\pi x)}, \quad q(x,0) = \sin(\cos(2\pi x)), \quad B(x) = \sin^2(\pi x),$$

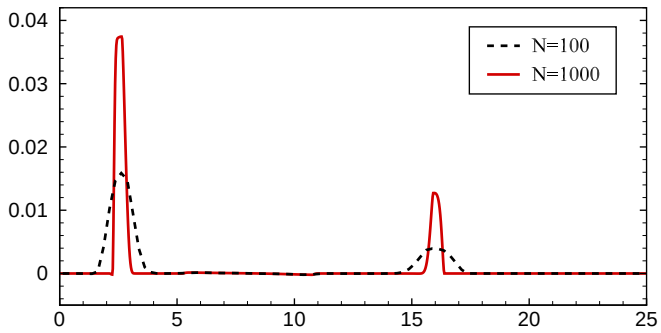

Figure 4.6: Example 2, Case (b): The difference between h and the background moving steady-state water depth computed using 100 and 1000 uniform cells.

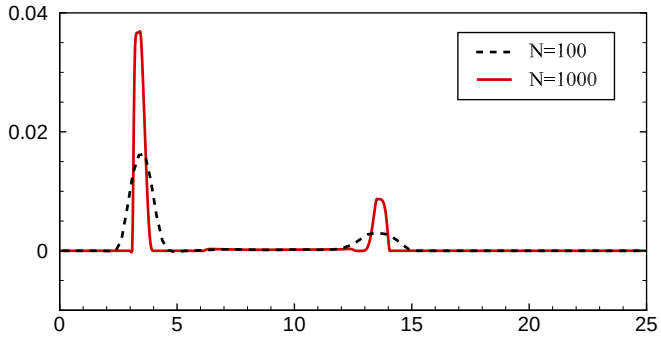

Figure 4.7: Example 2, Case (c): The difference between h and the background moving steady-state water depth computed using 100 and 1000 uniform cells.

are defined over the computational domain $[0, 1]$, and the periodic boundary conditions are imposed. Since the exact solution is not explicitly known, we use a numerical solution computed on a very fine mesh with $N = 8000$ uniform grid cells as a reference solution. We run the simulations until the final time $t = 0.1$ when the solution is still smooth (shocks are developed later in time). In this test, we set $a = 10$.

We measure the L^1-errors for both h and q over different grid sizes. The results are reported on Table 4.1, where one can observe the second order of accuracy as expected.

Number of	h		q	
grid cells	L^1-error	Rate	L^1-error	Rate
200	1.05e-03	–	9.27e-03	–
400	2.66e-04	1.99	2.19e-03	2.08
800	6.47e-05	2.04	5.27e-04	2.06
1600	1.59e-05	2.02	1.26e-04	2.06
3200	4.27e-06	1.90	2.75e-05	2.20

Table 4.1: Example 3: L^1-errors and experimental convergence rates.

Example 4—Convergence to Steady States (Continuous Bottom Topography)

This is a modification of Example 1 with the only difference that we now take into account the Manning friction term. We still consider the same super-, sub- and transcritical cases with the initial and boundary conditions (4.2), (4.3) and (4.5), respectively.

In all of these three cases, the numerical solutions are obtained by the proposed partial relaxation scheme at time $t = 300$ using 200 uniform cells. The obtained results ($h + B$, q and K) are shown in Figures 4.8–4.10. As one can see, the proposed numerical scheme can capture the steady states of different flow regimes in the presence of bed friction.

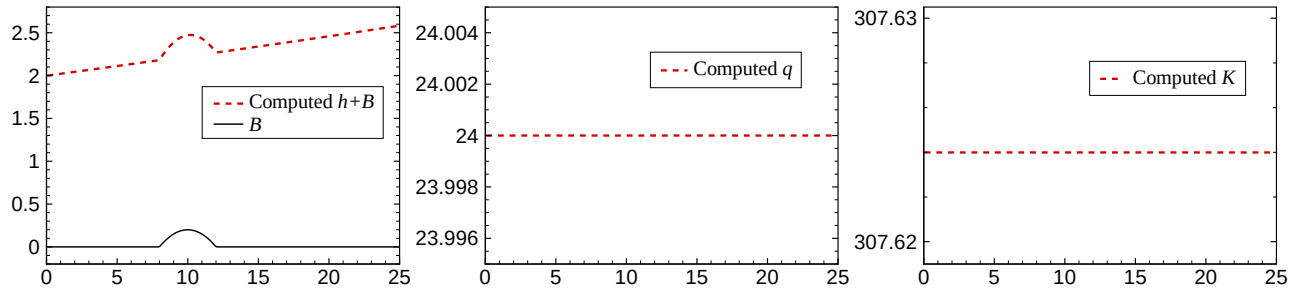

Figure 4.8: Example 4, Case (a): Computed $h + B$, q and K.

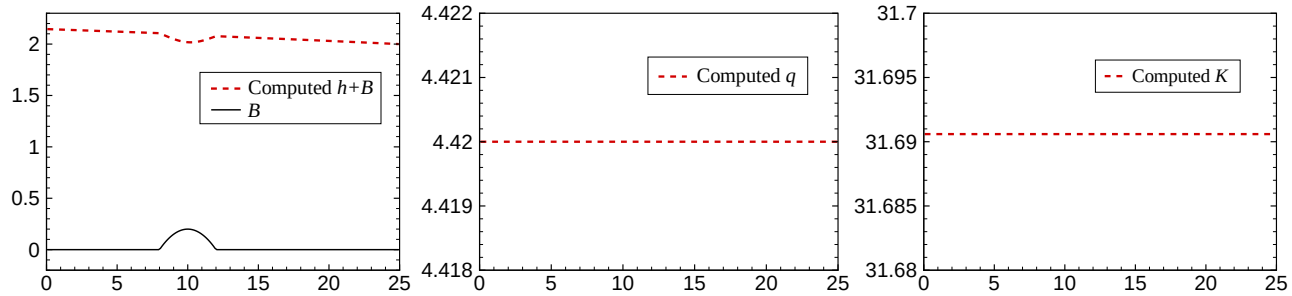

Figure 4.9: Example 4, Case (b): Computed $h + B$, q and K.

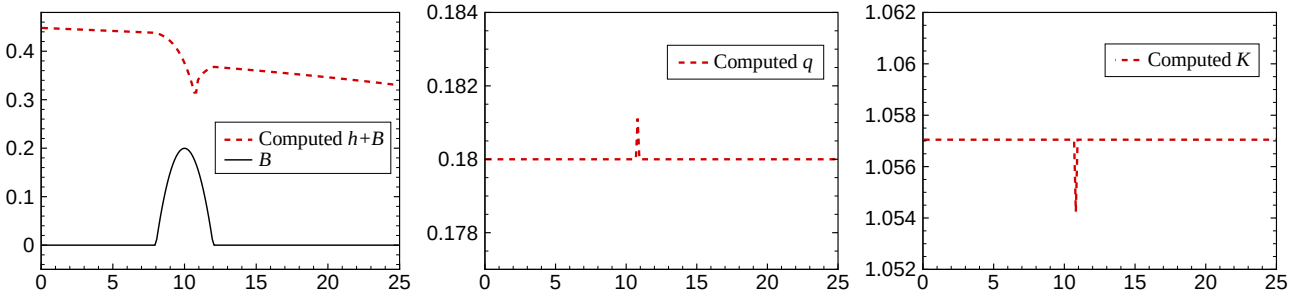

Figure 4.10: Example 4, Case (d): Computed $h + B$, q and K.

Example 5—Small Perturbations of Moving-Water Equilibria (Continuous Bottom Topography)

In this example, we test the ability of the proposed partial relaxation scheme of capturing the propagation of small perturbations of the moving-water equilibria. We consider the same bottom topography function (4.1) and the initial data are obtained by adding a small positive number 0.001 to the water depth in the interval $x \in [4.5, 5.5]$ to the steady-state solutions obtained in Cases (a) and (b) in Example 4.

We compute the numerical solutions until the final times $t = 1$ in Case (a) and $t = 1.5$ in Cases (b) using coarse and fine meshes with 100 and 1000 uniform cells, respectively. The obtained results are shown in Figures 4.11 and 4.12, where one can observe that no spurious oscillations are generated.

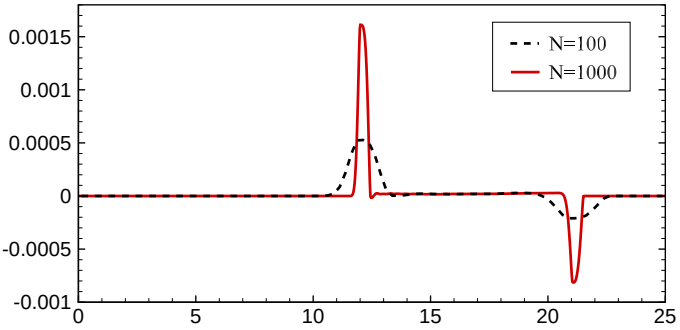

Figure 4.11: Example 5, Case (a): The difference between h and the background moving steady-state water depth computed using 100 and 1000 uniform cells.

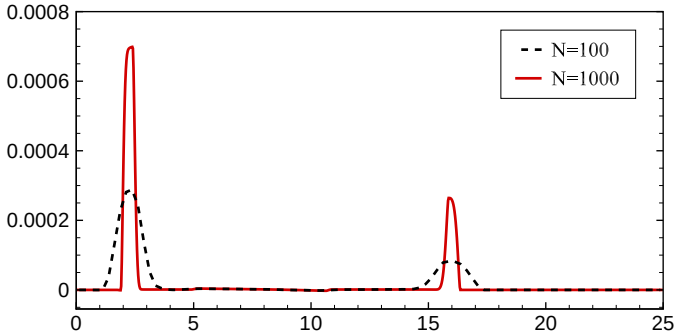

Figure 4.12: Example 5, Case (b): The difference between h and the background moving steady-state water depth computed using 100 and 1000 uniform cells.

Example 6—Convergence to Steady States (Discontinuous Bottom Topography)

Next, we numerically study the convergence towards a steady flow over a discontinuous bump. The bottom topography is given by

$$B(x) = \begin{cases} 0.2, & \text{if } \ 8 \le x \le 12, \\ 0, & \text{otherwise.} \end{cases} \tag{4.6}$$

We consider the same super-, sub- and transcritical cases with the initial and boundary conditions (4.2), (4.3) and (4.5), respectively. In all of these three cases, the numerical solutions are obtained by the proposed partial relaxation scheme at time $t = 300$ using 200 uniform cells.

The obtained results ($h + B$, q and K) are shown in Figures 4.13–4.15. As one case see, in Cases (a) and (b), the quality of the obtained results is practically not affected by the presence of the discontinuity in B, while in the transcritical Case (d), somewhat larger (compared to Example 4) jumps in q and K at the flow regime transition location near $x = 12$ can be observed. Yet, one can conclude that the proposed numerical scheme is capable of capturing the steady states of different flow regimes over the discontinuous bottom bed.

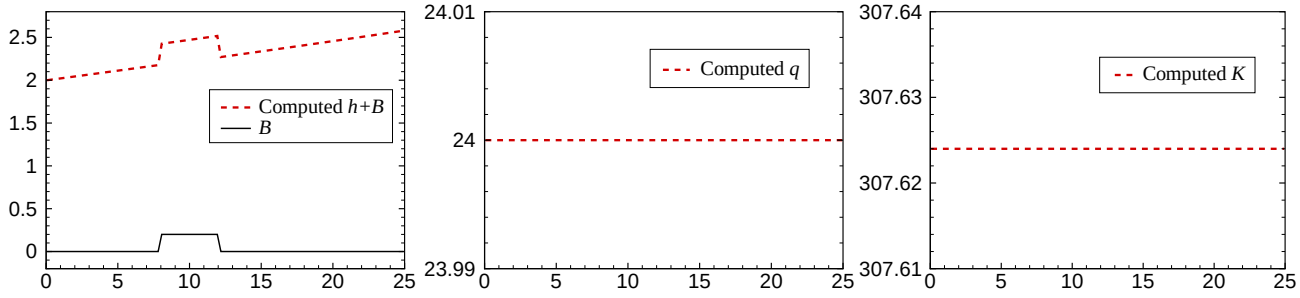

Figure 4.13: Example 6, Case (a): Computed $h + B$, q and K.

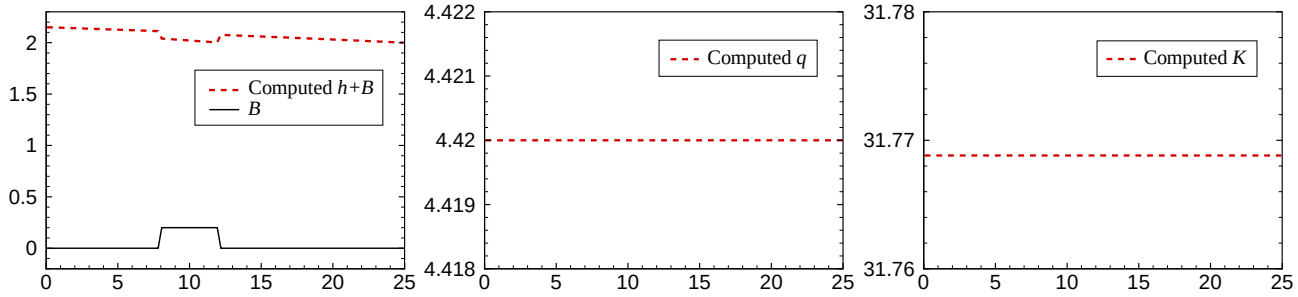

Figure 4.14: Example 6, Case (b): Computed $h + B$, q and K.

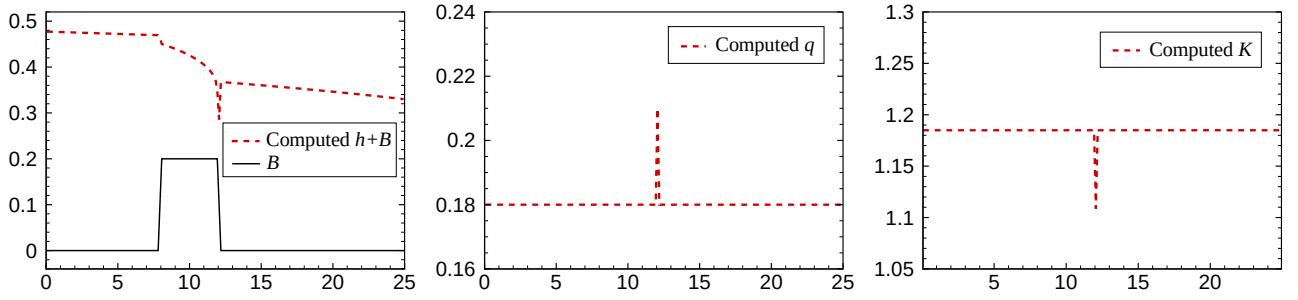

Figure 4.15: Example 6, Case (d): Computed $h + B$, q and K.

Example 7—Small Perturbations of Moving-Water Equilibria (Discontinuous Bottom Topography)

In this example, we investigate the ability of the proposed partial relaxation scheme to capture small perturbations of the moving-water equilibria over the discontinuous bottom topography given by (4.6). The initial data are obtained by adding a small positive number 0.001 to the water depth in the interval $x \in [5.75, 6.25]$ to the steady-state solutions obtained in Cases (a) and (b) in Example 6. In this test, we compute the solutions until the final times $t = 1$ in Case (a) and $t = 1.5$ in Case (b) using either 100 or 1000 uniform grid cells. The obtained results, reported in Figures 4.16 and 4.17, demonstrate that in the case of discontinuous B, the proposed numerical scheme is able to capture small perturbations of the moving-water steady state in a non-oscillatory manner.

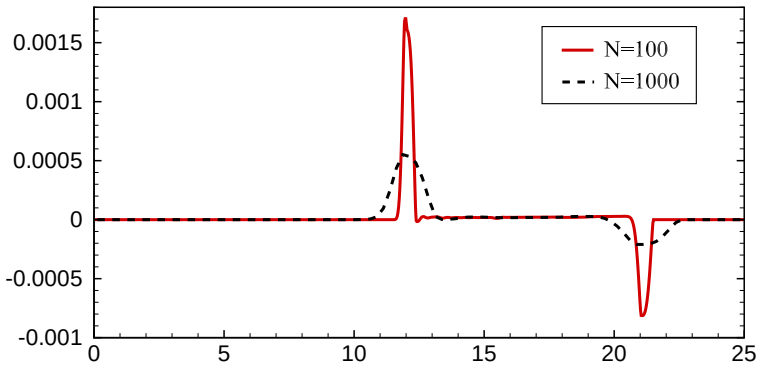

Figure 4.16: Example 7, Case (a): The difference between h and the background moving steady-state water depth computed using 100 and 1000 uniform cells.

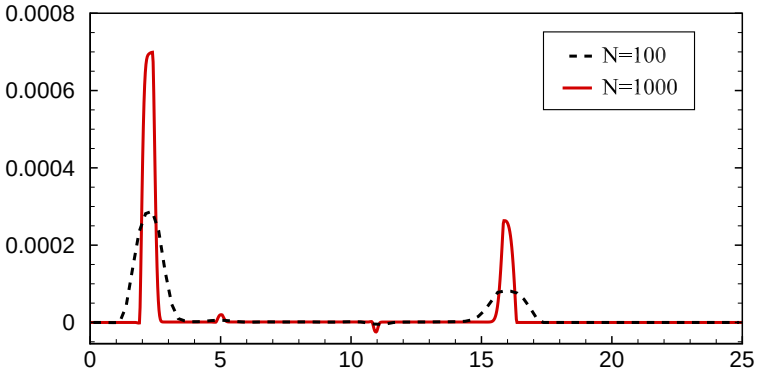

Figure 4.17: Example 7, Case (b): The difference between h and the background moving steady-state water depth computed using 100 and 1000 uniform cells.

Example 8—Riemann Problem

In the final example, we test the performance of the proposed partial relaxation scheme on the test problem with a dry bed by numerically solving the initial value problem with the following

Riemann initial data:

$$h(x,0)=\begin{cases}2, & \text{if } x<5,\\ 0, & \text{otherwise,}\end{cases}\qquad q(x,0)=\begin{cases}24, & \text{if } x<5,\\ 0, & \text{otherwise,}\end{cases}$$

and the same bottom topography and boundary conditions as in Example 1, Case (a). We compute the solution using 100 uniform grid cells and plot its snapshots at times $t = 0.1$, 0.5, 1, 2 and 5 in Figure 4.18. One can observe that the obtained results are stable, the water flow runs through the bump and by $t = 5$ it reaches the same steady state as in Example 5, Case (a) as expected.

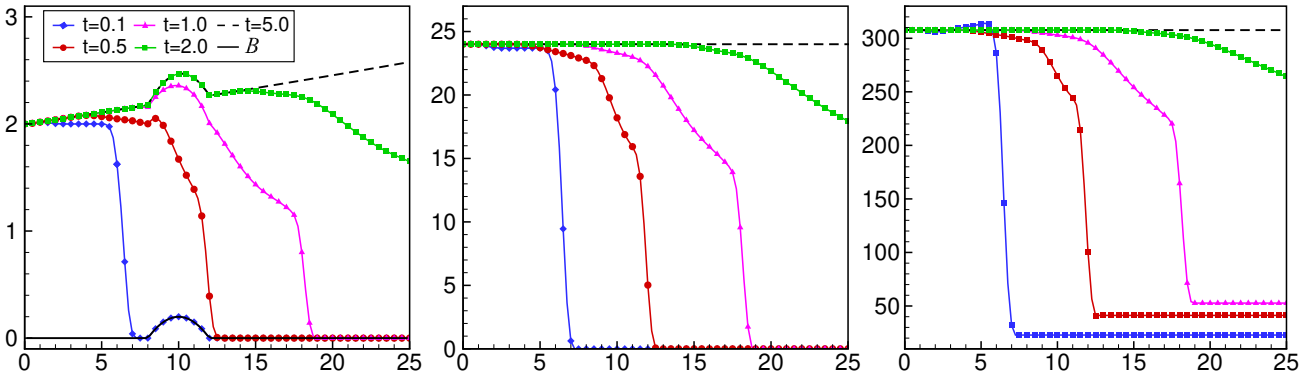

Figure 4.18: Example 8: Computed $h + B$ (left), q (middle) and K (right).

Acknowledgments. We would like to thank Dr. Theodoros Katsaounis for fruitful discussions and helpful comments. The work of S. Jin was supported in part by NSFC grants 31571071 and 11871297. The work of A. Kurganov was supported in part by NSFC grant 11771201 and NSF grants DMS-1521009 and DMS-1818666.

References

[1] E. Audusse, F. Bouchut, M.-O. Bristeau, R. Klein, and B. Perthame, *A fast and stable well-balanced scheme with hydrostatic reconstruction for shallow water flows*, SIAM J. Sci. Comput., 25 (2004), pp. 2050–2065.

[2] A. Bollermann, G. Chen, A. Kurganov, and S. Noelle, *A well-balanced reconstruction of wet/dry fronts for the shallow water equations*, J. Sci. Comput., 56 (2013), pp. 267–290.

[3] A. Bollermann, S. Noelle, and M. Lukáčová-Medviďová, *Finite volume evolution Galerkin methods for the shallow water equations with dry beds*, Commun. Comput. Phys., 10 (2011), pp. 371–404.

[4] F. Bouchut and T. Morales de Luna, *A subsonic-well-balanced reconstruction scheme for shallow water flows*, SIAM J. Numer. Anal., 48 (2010), pp. 1733–1758.

[5] M. J. Castro Díaz, J. A. López-García, and C. Parés, *High order exactly well-balanced numerical methods for shallow water systems*, J. Comput. Phys., 246 (2013), pp. 242–264.

[6] L. Cea and M. E. Vázquez-Cendón, *Unstructured finite volume discretisation of bed friction and convective flux in solute transport models linked to the shallow water equations*, J. Comput. Phys., 231 (2012), pp. 3317–3339.

[7] S. Chapman and T. G. Cowling, *The mathematical theory of non-uniform gases. An account of the kinetic theory of viscosity, thermal conduction and diffusion in gases*, Third edition, prepared in co-operation with D. Burnett, Cambridge University Press, London, 1970.

[8] Y. Cheng, A. Chertock, M. Herty, A. Kurganov, and T. Wu, *A new approach for designing moving-water equilibria preserving schemes for the shallow water equations*, J. Sci. Comput. To appear.

[9] Y. Cheng and A. Kurganov, *Moving-water equilibria preserving central-upwind schemes for the shallow water equations*, Commun. Math. Sci., 14 (2016), pp. 1643–1663.

[10] A. Chertock, S. Cui, A. Kurganov, c. N. Özcan, and E. Tadmor, *Well-balanced schemes for the Euler equations with gravitation: Conservative formulation using global fluxes*, J. Comput. Phys., 358 (2018), pp. 36–52.

[11] A. Chertock, S. Cui, A. Kurganov, and W. Tong, *Steady state and sign preserving semi-implicit Runge-Kutta methods for ODEs with stiff damping term*, SIAM J. Numer. Anal., 53 (2015), pp. 1987–2008.

[12] A. Chertock, S. Cui, A. Kurganov, and T. Wu, *Well-balanced positivity preserving central-upwind scheme for the shallow water system with friction terms*, Internat. J. Numer. Meth. Fluids, 78 (2015), pp. 355–383.

[13] A. Chertock, M. Dudzinski, A. Kurganov, and M. Lukáčová-Medviďová, *Well-balanced schemes for the shallow water equations with Coriolis forces*, Numer. Math., 138 (2018), pp. 939–973.

[14] A. Chertock, M. Herty, and c. N. Özcan, *Well-balanced central-upwind schemes for* 2×2 *systems of balance laws*, in Theory, Numerics and Applications of Hyperbolic Problems I, vol. 236 of Springer Proceedings in Mathematics & Statistics, Springer, 2018, pp. 345–361.

[15] F. Coquel and B. Perthame, *Relaxation of energy and approximate Riemann solvers for general pressure laws in fluid dynamics*, SIAM J. Numer. Anal., 35 (1998), pp. 2223–2249.

[16] A. J. C. de Saint-Venant, *Thèorie du mouvement non-permanent des eaux, avec application aux crues des rivière at à l'introduction des marèes dans leur lit.*, C.R. Acad. Sci. Paris, 73 (1871), pp. 147–154, 237–240.

[17] A. I. Delis and T. Katsaounis, *Relaxation schemes for the shallow water equations*, Internat. J. Numer. Methods Fluids, 41 (2003), pp. 695–719.

[18] J. M. Gallardo, C. Parés, and M. Castro, *On a well-balanced high-order finite volume scheme for shallow water equations with topography and dry areas*, J. Comput. Phys., 227 (2007), pp. 574–601.

[19] L. Gosse, *A well-balanced flux-vector splitting scheme designed for hyperbolic systems of conservation laws with source terms*, Comput. Math. Appl., 39 (2000), pp. 135–159.

[20] S. Jin, *A steady-state capturing method for hyperbolic systems with geometrical source terms*, M2AN Math. Model. Numer. Anal., 35 (2001), pp. 631–645.

[21] S. Jin and X. Wen, *Two interface-type numerical methods for computing hyperbolic systems with geometrical source terms having concentrations*, SIAM J. Sci. Comput., 26 (2005), pp. 2079–2101.

[22] S. Jin and Z. P. Xin, *The relaxation schemes for systems of conservation laws in arbitrary space dimensions*, Comm. Pure Appl. Math., 48 (1995), pp. 235–276.

[23] A. A. Khan and W. Lai, *Modeling Shallow Water Flows using the Discontinuous Galerkin Method*, CRC Press, Taylor and Francis, New York, 2014.

[24] C. Klingenberg, A. Kurganov, and M. Zenk, *Moving-water equilibria preserving HLL-type schemes for the shallow water equations*. Preprint.

[25] A. Kurganov, *Finite-volume schemes for shallow-water equations*, Acta Numer., 27 (2018), pp. 289–351.

[26] A. Kurganov and D. Levy, *Central-upwind schemes for the Saint-Venant system*, M2AN Math. Model. Numer. Anal., 36 (2002), pp. 397–425.

[27] A. Kurganov, S. Noelle, and G. Petrova, *Semidiscrete central-upwind schemes for hyperbolic conservation laws and Hamilton-Jacobi equations*, SIAM J. Sci. Comput., 23 (2001), pp. 707–740.

[28] A. Kurganov and G. Petrova, *A second-order well-balanced positivity preserving central-upwind scheme for the Saint-Venant system*, Commun. Math. Sci., 5 (2007), pp. 133–160.

[29] R. J. LeVeque, *Balancing source terms and flux gradients in high-resolution Godunov methods: the quasi-steady wave-propagation algorithm*, J. Comput. Phys., 146 (1998), pp. 346–365.

[30] K.-A. Lie and S. Noelle, *On the artificial compression method for second-order nonoscillatory central difference schemes for systems of conservation laws*, SIAM J. Sci. Comput., 24 (2003), pp. 1157–1174.

[31] H. Nessyahu and E. Tadmor, *Nonoscillatory central differencing for hyperbolic conservation laws*, J. Comput. Phys., 87 (1990), pp. 408–463.

[32] S. Noelle, Y. Xing, and C.-W. Shu, *High-order well-balanced finite volume WENO schemes for shallow water equation with moving water*, J. Comput. Phys., 226 (2007), pp. 29–58.

[33] M. Ricchiuto and A. Bollermann, *Stabilized residual distribution for shallow water simulations*, J. Comput. Phys., 228 (2009), pp. 1071–1115.

[34] G. Russo, *Central schemes for conservation laws with application to shallow water equations*, in Trends and Applications of Mathematics to Mechanics, Springer Milan, 2005, pp. 225–246.

[35] G. Russo and A. Khe, *High order well-balanced schemes based on numerical reconstruction of the equilibrium variables*, in Proceedings "WASCOM 2009" 15th Conference on Waves and Stability in Continuous Media, World Sci. Publ., Hackensack, NJ, 2010, pp. 230–241.

[36] I. Suliciu, *On the thermodynamics of rate-type fluids and phase transitions. I. Rate-type fluids*, Internat. J. Engrg. Sci., 36 (1998), pp. 921–947.

[37] P. K. Sweby, *High resolution schemes using flux limiters for hyperbolic conservation laws*, SIAM J. Numer. Anal., 21 (1984), pp. 995–1011.

[38] B. van Leer, *Towards the ultimate conservative difference scheme. V. A second-order sequel to Godunov's method*, J. Comput. Phys., 32 (1979), pp. 101–136.

[39] M. E. Vázquez-Cendón, *Improved treatment of source terms in upwind schemes for the shallow water equations in channels with irregular geometry*, J. Comput. Phys., 148 (1999), pp. 497–526.

[40] Y. Xing, *Exactly well-balanced discontinuous Galerkin methods for the shallow water equations with moving water equilibrium*, J. Comput. Phys., 257 (2014), pp. 536–553.

[41] Y. Xing and C.-W. Shu, *A survey of high order schemes for the shallow water equations*, J. Math. Study, 47 (2014), pp. 221–249.

[42] Y. Xing, C.-W. Shu, and S. Noelle, *On the advantage of well-balanced schemes for moving-water equilibria of the shallow water equations*, J. Sci. Comput., 48 (2011), pp. 339–349.